ADVANCED MATERIALS INTERFACES
www.advmatinterfaces.de

Simultaneous Deconvolution of In-Plane and Out-of-Plane Forces of HOPG at the Atomic Scale under Ambient Conditions by Multifrequency Atomic Force Microscopy

*Anna L. Eichhorn and Christian Dietz**

Multifrequency atomic force microscopy (AFM) is shown to be an excellent tool for imaging crystal structures at atomic resolution in different spatial directions. However, determining the forces between single atoms remains challenging, particularly in air under ambient conditions. Developed here is a trimodal AFM approach that simultaneously acquires torsional and flexural frequency-shift images and spectroscopic data to transfer these observables into in-plane and out-of-plane forces between single bonds of highly oriented pyrolytic graphite (HOPG) at atomic resolution in air under ambient conditions based on the Fourier method. It is found that the cantilever mean deflection is an excellent indicator to understand that strong attractive interactions between the tip and the surface of HOPG in dynamic AFM imply a local lift of the topmost carbon layer when using higher eigenmodes for the topographical feedback. Cross-talk between torsional and flexural-oscillation modes is shown to be negligible. Interestingly, significant differences are observed in the in-plane forces depending on the orientation of the carbon bonds relative to the direction of torsional oscillation.

1. Introduction

Highly oriented pyrolytic graphite (HOPG) is well known as atomically flat substrate for various experimental setups and advanced sensors.[1, 2] Graphene, the basal plane of HOPG, has been shown to be a promising material as membrane or for future applications, such as in electronics.[3] However, although there have been some studies of how defects affect the nanomechanical properties of graphene,[4–6] it remains challenging to analyze the local effect of different types of defects on the in-plane and out-of-plane elastic properties at the atomic level. Also, because graphene devices are exposed to environmental influences, measurements in air under ambient conditions are more relevant than those under ultrahigh vacuum (UHV). While imaging graphitic surfaces at the atomic scale has become a standard procedure using atomic force microscopy (AFM) under UHV,[7] at low temperatures[8–11] or in a liquid environment[12] it remains a challenging task to obtain comparable high resolution in air under ambient conditions.

In 2014, Wastl et al. were the first to demonstrate atomic resolution of HOPG in air under ambient conditions, using stiff quartz tuning-fork force sensors (qPlus sensors[13]) in the flexural-frequency modulation mode.[14] A major advantage of using qPlus sensors is that they allow the cantilever to oscillate with ultrasmall amplitudes (<1 nm) because of their high stiffness. However, although the combination of in-plane and out-of-plane oscillation modes is feasible, the implementation is not straightforward because qPlus sensors require some nonstandard AFM equipment.[15–17] Another option for achieving ultrasmall oscillation amplitudes is to exploit higher flexural cantilever eigenmodes because they are stiffer than the fundamental eigenmode. Atomic resolution has been shown successfully on different substrates in air when higher eigenmodes were used for the amplitude or frequency-shift feedback.[18–20] Multifrequency AFM has also been shown to be capable of atomic-resolution imaging using the first and second flexural eigenmodes.[7,21,22] Also, some research groups have achieved atomic resolution with flexural–torsional approaches, but not under ambient conditions.[7,23] Most of the benchmark images in terms of high resolution were obtained with CO-functionalized tips,[24,25] but unfortunately they cannot be used in air under ambient conditions, and they suffer from bending while imaging.[26] Although there are several approaches for imaging with atomic resolution, determining forces remains a challenging task if measurements are performed in air under ambient conditions. In water under UHV and/or low temperatures, out-of-plane forces have been determined successfully with atomic resolution in spectroscopic experiments,[27–31] but unfortunately it is challenging to obtain atomic resolution in air under ambient conditions with spectroscopic mapping because of long image-acquisition times and the associated thermal drift that is substantial when imaging at the atomic scale. Recently, Seeholzer et al. developed an approach to deconvoluting forces from lateral

A. L. Eichhorn, C. Dietz
Physics of Surfaces
Institute of Materials Science
Technische Universität Darmstadt
Alarich-Weiss-Str. 2, 64287 Darmstadt, Germany
E-mail: dietz@pos.tu-darmstadt.de

The ORCID identification number(s) for the author(s) of this article can be found under https://doi.org/10.1002/admi.202101288.

DOI: 10.1002/admi.202101288

frequency-shift images at the molecular level using the Fourier method.[32] The advantage of this method over others is that the force determination from a single image is much faster than that from a complete set of spectroscopic data. Because of the applicability to single images, the method is assumed to be particularly suitable for force deconvolution in air under ambient conditions. To date, the Fourier method has been used for only in-plane force determination.

In the present work, we extend the method to determine in-plane and out-of-plane forces simultaneously from torsional and flexural frequency-shift data, respectively, to unravel the interactions between single carbon atoms of HOPG in air under ambient conditions. For acquiring atomically resolved images, we have developed a trimodal approach[33,34] based on the AMFlex-FMTor method[35] demonstrated by Dietz. This mode uses photothermal excitation to drive the cantilever.[36,37] The blue excitation laser spot is placed at the fixed end of the cantilever but at a considerable distance from the length symmetry axis.[23] This enables the simultaneous excitation of flexural and torsional eigenmodes by modulating the power of the laser periodically with frequencies matching the flexural and torsional resonance frequencies. The first flexural-eigenmode amplitude of the cantilever is used for topographical feedback (AMFlex). Hence, by adjusting the flexural-amplitude setpoint, the indentation into the sample can be controlled. From the resulting phase shift between oscillation and excitation, dissipative sample properties in the out-of-plane direction can be obtained. Additionally, a phase-locked loop (PLL) is used to frequency-modulate the torsional oscillation of the cantilever (FMTor). Thus, the torsional phase shift is always kept at 90° to maintain the oscillation at resonance when the tip interacts with the surface. Additionally, the torsional oscillation amplitude is kept constant by adjusting the drive amplitude. From the drive amplitude, dissipative information about the in-plane sample properties can be deduced. The frequency shift of the torsional oscillation provides information about the elasticity of the sample in its in-plane direction.[35] Applying the described method for stiff samples such as HOPG requires some modifications of the setup as shown in **Figure 1**. To achieve a 3D analysis of the interacting forces, the method was extended to a trimodal setup, where the second flexural eigenmode was used for the topographic feedback in amplitude modulation (AMFlex2), the frequency-modulated torsional oscillation (FMTor1) provided access to the in-plane forces and the frequency-modulated third-eigenmode flexural oscillation (FMFlex3) gave access to the out-of-plane forces.

Inspired by Kawai et al.[18] and Korolkov et al.,[20] we use the amplitude of the second flexural eigenmode for the topographical feedback to take advantage of the fact that this particular eigenmode is stiffer than the fundamental eigenmode. In combination with the small amplitude small setpoint (SASS) method introduced by Santos et al.,[38] we reach a sufficiently small tip–sample distance to routinely achieve atomic resolution on HOPG surfaces. To sense in-plane and out-of-plane forces simultaneously, we also excite the third flexural eigenmode oscillation. Similar to the torsional eigenmode, the third flexural eigenmode is driven as frequency-modulated in constant-amplitude mode to establish a second PLL circuit. Hereinafter, according to the excited modes and feedbacks, we designate the mode as the AMFlex2-FMTor1-FMFlex3 mode. The advantages of amplitude modulation for feedback control over other methods are straightforward implementation, stable operation, and fast response in air under ambient conditions.[39]

2. Results and Discussion

2.1. Trimodal Imaging in AMFlex2-FMTor1-FMFlex3 Mode

Figure 2 shows AFM images of HOPG taken simultaneously in the AMFlex2-FMTor1-FMFlex3 mode. Atomic contrast is

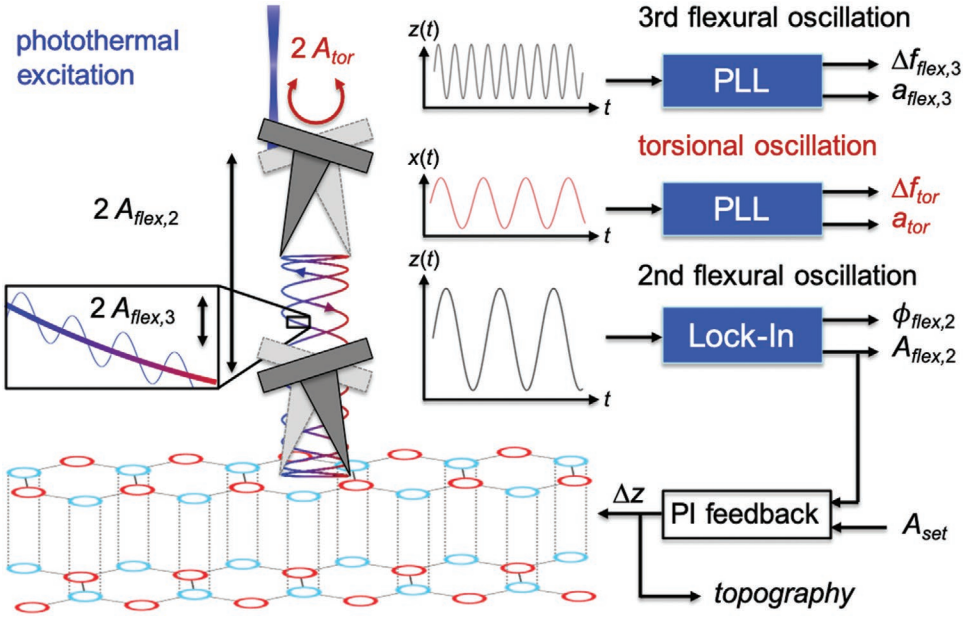

Figure 1. Schematic of AMFlex2-FMTor1-FMFlex3 mode for atomic-resolution imaging of HOPG. Out-of-plane forces can be determined from the third-eigenmode flexural frequency shift, whereas in-plane forces can be calculated from the torsional-eigenmode frequency shift.

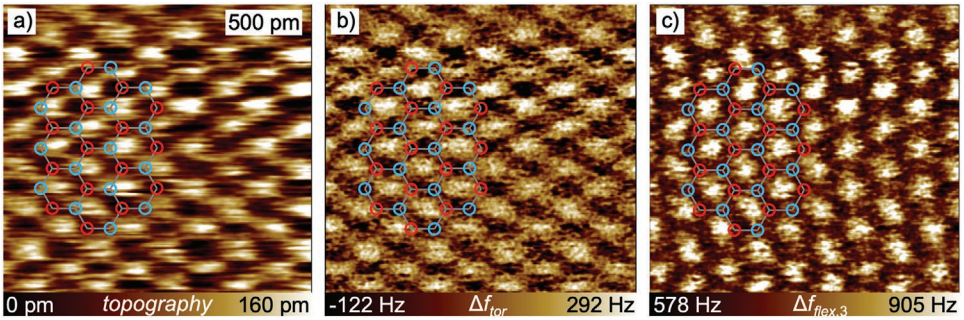

Figure 2. AFM images of HOPG taken in AMFlex2-FMTor1-FMFlex3 mode: a) topography image, and b) torsional and c) flexural frequency-shift images. Imaging parameters: $A_{0(flex,2)}$ = 770 pm, $A_{flex,2}$ = 100 pm, A_{tor} = 80 pm, $A_{flex,3}$ = 220 pm.

observed in a) the topography image and b) the torsional and c) third-eigenmode flexural frequency-shift images, in which the atoms appear as dark spots and the hollow sides as bright protrusions. In the topography image (Figure 2a) and the torsional frequency-shift image (Figure 2b) we did not observe the honeycomb structure of HOPG, whereas the third-eigenmode frequency-shift image (Figure 2c) resolves carbon hexagons, however, compared to the high quality images shown by Wastl et al.[14] with inverted contrast (see Figure S1 in the Supporting Information for an inverted image to compare). This inverted contrast is well known for AFM imaging in frequency-modulation mode when operating the instrument in the attractive regime.[7,10] Nevertheless, in our case the assignment of atomic sides requires some further explanation because both the third-eigenmode frequency-shift image shown in Figure 2c and the phase of the second-eigenmode oscillation (not shown) suggest that imaging was performed in the repulsive regime. Also, we observed a small offset between the frequency-shift images and the topography image along the fast scan axis, as well as an unexpected high corrugation of up to 160 pm peak-to-peak. We found that these effects can be attributed to a significant mean deflection of the cantilever during imaging with topographic feedback on a higher eigenmode.[40,41] Details about the relationship between mean deflection and contrast formation are given in Figure S2 in the Supporting Information.

2.2. Dynamic Spectroscopy in AMFlex2-FMTor1-FMFlex3 Mode

To clarify further the contrast formation of the atomically resolved images in Figure 2, we performed dynamic spectroscopy experiments at the alleged carbon-atom location on HOPG using the AMFlex2-FMTor1-FMFlex3 mode. Therefore, the amplitude feedback was turned off and the amplitude of the second flexural eigenmode oscillation was free to change upon approach and retract while triggering at 10% of the free oscillation amplitude (determined at 200 nm above the surface). Besides the change in the second-eigenmode amplitude, we also recorded the changes in the second-eigenmode phase, the mean deflection, the third-eigenmode frequency shift, and the torsional frequency shift as functions of the tip–sample distance *d*. The results are shown in **Figure 3**a, and details about the calibration of the different

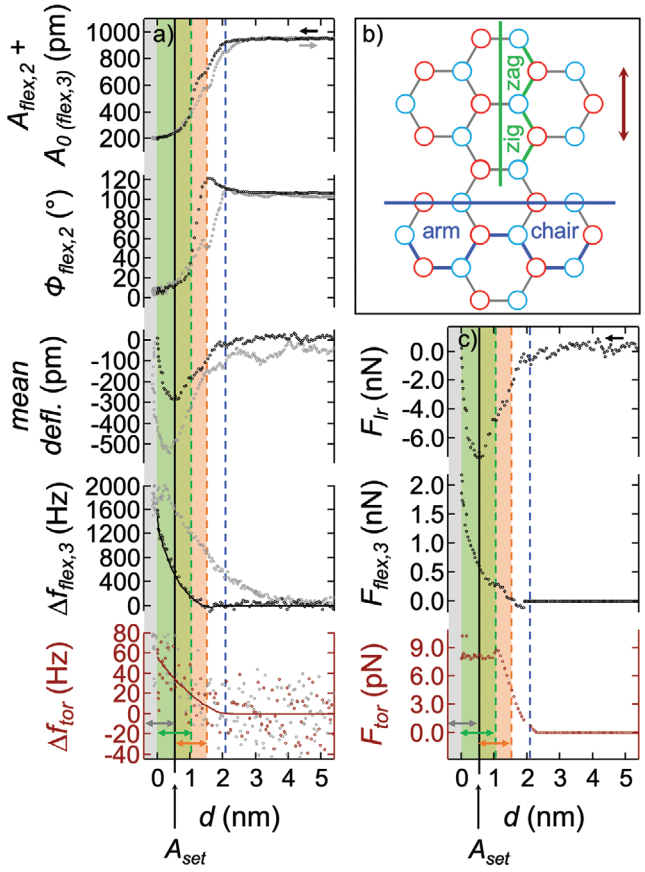

Figure 3. Dynamic spectroscopy at alleged carbon-atom location of HOPG in air under ambient conditions. a) Amplitude, phase, mean deflection, and flexural and torsional frequency shifts versus tip–sample distance *d*. The approach curves are shown in black/red (flexural/torsional), the retract curves are shown in gray, and the solid lines represent the fitted frequency-shift data of the approach curves. b) Scheme of zigzag and armchair orientation of carbon hexagons. Here, the torsional oscillation direction (red double-headed arrow) is along the zigzag direction of the hexagonal carbon structure. c) Long-range interaction F_{lr} between tip and sample calculated from mean deflection and force deconvolution from fitted flexural and torsional frequency-shift data (solid lines in (a)) using the Sader method. The setpoint amplitude at which images were taken is marked by the black vertical lines. Some characteristic regions of the approach curves are colored gray, green, and orange and marked by double-headed arrows. The dashed vertical lines mark the starts of the characteristic areas.

eigenmode amplitudes and the deflection are given in the Supporting Information.

Figure 3a shows hysteresis between the approach and retract curves, which we attribute on the one hand to the existence of water layers covering the surfaces at both sides, tip and sample. On the other hand, we assume that a significant portion of the hysteresis is caused by the local lift of the topmost carbon layers.[42] The assumption was corroborated by comparative spectroscopic measurements performed on HOPG and silicon as shown in Figure S3 in the Supporting Information. We have marked some characteristic regions of the approach curves as colored areas separated by dashed lines. Starting from the largest tip–sample distance (right side of the graph), the blue dashed line marks the onset of attractive forces at ≈2 nm from the surface, which results in a reduction of the second flexural amplitude and the mean deflection and an increase in the second flexural phase. While the third-eigenmode frequency stays at initial resonance, a small increase in the torsional frequency shift is noticeable from the fit of the original data (solid line), but with a high uncertainty as can be estimated from the scattered data points. Here, the torsional oscillation direction was along the zigzag orientation of the carbon hexagons, as shown schematically in Figure 3b. The orange dashed line at ≈1.5 nm from the sample surface marks the maximum attractive force sensed by the tip, notable for the second-flexural-eigenmode phase shift that results in a significant change of the gradient of the second-flexural-eigenmode amplitude. At that point, the mean–deflection changes in gradient, which can be interpreted as an increase in the average attractive force, whereas the third-eigenmode frequency shift starts to increase (stronger repulsion). The average torsional frequency shift starts to increase when the tip is moved closer than 2 nm to the surface. The green line at a tip–sample distance of ≈1 nm marks where the approach curve coincides with the retract curve for the second-eigenmode amplitude and phase upon approach, although we noticed large hysteresis for the mean deflection and the third-eigenmode frequency shift. While the gradient of the decreasing mean deflection remains constant, that of the third flexural frequency shift again increases. The minimum mean cantilever deflection is reached at the second-eigenmode amplitude setpoint marked by the black dashed line. Consequently, for smaller tip–sample distances, the mean deflection and the third-eigenmode frequency shift both increase, but the mean deflection remains predominantly attractive.

From these observations, we conclude that using the AMFlex2-FMTor1-FMFlex3 setup provides three different overlapping contrast regimes, which are marked in gray ($d < 0.5$ nm), green ($d \approx$ 0–1 nm), and orange ($d \approx$ 0.5–1.5 nm) in Figure 3a. In the orange regime, the gradients of the mean deflection and third-flexural-eigenmode frequency shift show opposite trends, whereas at closer tip–sample distances (gray) the trends coincide. The green regime represents the area close to the minimum mean cantilever deflection, i.e., the sign of the gradient might differ between the atomic sites. We were able to show that a variation of the third-eigenmode oscillation amplitude enables imaging in the three different described contrast-formation regimes (see Figure S4 in the Supporting Information for details). This implies that imaging in the gray (resp. orange) area results in equal (resp. inverted) contrasts of the mean–deflection and third-eigenmode frequency-shift images. For images taken in the green area, we expect differently pronounced offsets between the maxima and minima of the mean deflection and the third-eigenmode frequency shift. At the same time, we observed that the mean–deflection images and the topography images show nearly the same patterns, however, with inverted contrast. Hence, the topography signal seems to be strongly influenced by the mean cantilever deflection during imaging, which might explain on the one hand the unexpected high corrugation of the atomic structure of HOPG in Figure 2a and on the other hand the small lateral offset between the topography image (Figure 2a) and the torsional and flexural frequency-shift images (Figure 2b,c). However, due to the fact that the spectroscopy and imaging measurements cannot be accomplished simultaneously, a direct proof of the hypothesis remains challenging. With the knowledge gained from the spectroscopic experiments, we conclude that for the images shown in Figure 2, the tip–sample distance was most likely in the range of 0–1 nm around the minimum mean deflection. This could have caused the small offset in the observed structure between the topography and frequency-shift images on the one hand and the appearance of hollow sides as maxima and the atoms as minima in the frequency-shift images on the other hand, although positive frequency shifts imply imaging in the repulsive regime. Additionally, we assume that imaging is influenced by a local lift of the topmost carbon layer, as suggested by the retract curves.

2.3. Force Reconstruction Using Sader Method

Having clarified the contrast formation, we seek quantities that are physically more meaningful, such as the forces between the different carbon atoms. From the mean–deflection signal, we can simply approximate the average long-range attractive force F_{lr} by multiplication with the static force constant. More meaningful short-range forces can be determined from the frequency-shift data. There are two standard approaches to quantifying forces from the frequency-shift data of FM-AFM measurements: the Sader method[43] developed by Sader and Jarvis and the matrix method[44] developed by Giessibl. The Sader method is based on a Laplace transform and uses the large-amplitude approximation—which presumes that the oscillation amplitude is larger than the characteristic length scale of the interaction force—to reconstruct forces by inverting the frequency-shift data. The matrix method is based on a transformation matrix that converts the frequency-shift data into forces. Both methods rely on the frequency-modulation mode with constant oscillation amplitude. Because the amplitude of the second flexural eigenmode is smaller than that of the third eigenmode at tip–sample distances that are relevant for imaging, we assume that the standard force-deconvolution methods are valid for the present imaging conditions after modifying the equations slightly. This modification is based on the observation that the height signal is dominated by the mean cantilever deflection and so the corrected tip–sample distance can be approximated as a constant height, similar to the situation in frequency modulation. Unlike frequency modulation, we must consider the

varying oscillation amplitude upon approach, whereupon the modified version of the formula derived by Sader and Jarvis[45] is given by

$$F_{\text{flex},3}(d) = k_{\text{flex},3}\sqrt{2\pi\left(A_{\text{flex},2}(d) + A_{0(\text{flex},3)}\right)^3}\, D_{-}^{1/2}\frac{\Delta f_{\text{flex},3}(d)}{f_{0(\text{flex},3)}} \quad (1)$$

where $k_{\text{flex},3}$ is the stiffness of the third flexural eigenmode, $A_{\text{flex},2}$ is the tip–sample-distance-dependent amplitude of the second flexural eigenmode, $A_{0(\text{flex},3)}$ is the amplitude setpoint of the third flexural eigenmode, and $\Delta f_{\text{flex},3}$ and $f_{0(\text{flex},3)}$ are the frequency shift and resonance frequency, respectively, of the third flexural eigenmode. The force deconvolution uses the half-fractional derivative $D_{-}^{1/2}$ applied to the frequency-shift data.[46]

Several authors have shown that for bimodal AFM, the formula for calculating forces from frequency-shift data differs for the first and second eigenmodes.[7,21,46–48] From considering the amplitude ratios, we assume that we can treat the system as a bimodal AFM setup with both flexural eigenmodes (plus torsional eigenmode) being frequency-modulated. The corresponding formula has been shown to be valid for both flexural–flexural[21] and flexural–torsional[7] setups. The modified formula for determining the torsional force can be expressed as

$$F_{\text{tor}}(d) = 2k_{\text{tor}}\sqrt{2\pi\left(A_{\text{flex},2}(d) + A_{0(\text{flex},3)}\right)}\, I_{-}^{1/2}\frac{\Delta f_{\text{tor}}(d)}{f_{0(\text{tor})}} \quad (2)$$

where k_{tor} is the torsional stiffness, and Δf_{tor} and $f_{0(\text{tor})}$ are the frequency shift and resonance frequency, respectively, of the torsional eigenmode. Here, the force deconvolution relies on the half-fractional integral $I_{-}^{1/2}$ of the torsional frequency-shift data. Details about determining the underlying formula can be found in refs. [43,45,46], and information about implementing the formula in a MATLAB code is given in the Supporting Information.

The bimodal approach presumes that the two eigenmodes under consideration can oscillate independently of each other and that one oscillation amplitude is much smaller than the other. From dynamic spectroscopy with different oscillation amplitudes, we found no considerable coupling between the modes; potential cross-talk will be analyzed in more detail by means of imaging data. Also, note that calibrating the inverse optical lever sensitivity (invOLS) for the torsional eigenmode and the third flexural eigenmode is not straightforward (see the Supporting Information for details of the calibration). Despite the fact that the condition $A_{0(\text{flex},3)} >> A_{0(\text{tor})}$ might not be valid for every constellation of parameters, we assume that the bimodal approach can be used because of the spatial difference in oscillation direction.

The resulting forces after deconvolution of the fitted frequency-shift curves (solid lines in Figure 3a) are shown in Figure 3c. Additionally, the long-range forces determined from the mean–deflection curve in Figure 3a are plotted against the tip–sample distance. The strongest attractive force during approach is at a tip–sample distance of ≈500 pm and is 7.3 nN in absolute value. The strongest attractive force as determined from the retract curve is nearly twice as large (14 nN). Compared to the study by Chiesa and Lai,[49] who measured the attractive tip–sample forces under multiple aging conditions of HOPG, in the range of 0.7–1.3 nN, we found values that are approximately ten times higher. Calo et al.[50] observed an increase in the attractive force with increasing tip radius, which is unlikely to be the reason in our case. We assume that using diamond-like carbon (DLC) tips instead of the mostly used silicon tips might cause the higher tip–sample attraction originating from a larger Hamaker constant of DLC compared to that of silicon oxide.[51] The short-range flexural force ($F_{\text{flex},3}$) shows a similar trend to that of the third-eigenmode flexural frequency shift, although note a major difference in the region between the blue and orange dashed lines (tip–sample distance of 2–1.5 nm), where the short-range flexural force shows a small attractive region. During approach, starting from the orange dashed line, the repulsive force increases initially with a very small gradient. In the center between the orange and green dashed lines, note a jump to an overall repulsive force with a 250 pN increase in absolute value. Around the green dashed line, a small plateau of ≈500 pm width forms, where the repulsive force remains constant at 250 pN. Upon further approach, from $d < 750$ pm the force increases with increasing gradient. The maximum repulsive force reached is 2 nN, and the force at the setpoint amplitude is ≈480 pN. Interestingly, the in-plane force deduced from the torsional frequency shift increases constantly (tip–sample distance of 2–1 nm) up to a maximum repulsive value of ≈9 pN. The maximum torsional tip–sample force is reached at the position of the green dashed line, and further approach of the tip leads to a slightly decreased force plateau of 8 pN. Note the effects of this force behavior in the frequency-shift images: while the choice of the second-flexural-eigenmode amplitude setpoint influenced the torsional frequency-shift image only slightly, it had a clear influence on the third-eigenmode frequency-shift image. Details are given in Figure S5 in the Supporting Information.

Consequently, quantifying forces from dynamic spectroscopy data in the AMFlex2-FMTor1-FMFlex3 mode is indispensable for understanding contrast formation in images. Nevertheless, we encountered a few obstacles when using this method of force deconvolution with atomic resolution in air under ambient conditions. First, the determination of forces depends strongly on the actual tip–sample distance, thereby involving the correction for the mean deflection of the cantilever. The mean–deflection signal measured by the induced photocurrent on the photodiode is always accompanied by oscillations and/or tilt during approach and retract. Hence, the associated calibration is not straightforward and therefore prone to errors. This in turn influences the determination of all forces deduced from spectroscopy data. Second, hysteresis between approach and retract curves involves further sources of errors for the quantification. Third, the quantification of torsional forces is imprecise because of the high noise level of the frequency-shift data. Fourth, discriminating the atomic sides via dynamic spectroscopy at room temperature in air is challenging, a major cause being the influence of thermal drift. To the best of our knowledge, atomic-resolution dynamic spectroscopy in air under ambient conditions has not been demonstrated until now. For all these reasons, we decided to focus on a different approach suggested by Weymouth et al.[52] and Seeholzer et al.,[32] who

determined lateral tip–sample forces from dynamic lateral-force microscopy images using the Fourier method. This line-by-line approach relies on the same physical background as that of the Sader and matrix methods for force deconvolution from frequency-shift data. Consequently, we assume that our approximation of the setup as a trimodal one in frequency modulation is still reasonable. The Fourier method emerged because both standard methods can lead to errors in force deconvolution for certain force curves and amplitudes, in particular at the regions of local extrema.[53] Because of the substantial number of inflection points in our data, we decided to calculate forces based on the Fourier method with the images obtained on HOPG. It needs to be mentioned that the Fourier method is not applicable for the analysis of individual spectroscopy curves such as shown in Figure 3. For the acquirement of periodic structures necessary for the Fourier method, complete spectroscopic maps are needed. However, this is challenging on the atomic scale in air under ambient conditions due to thermal drift issues. Consequently, we cannot provide a direct comparison between the two reconstruction methods.

2.4. Force Reconstruction Using Fourier Method

The Fourier method bears the idea that a periodic function such as the lateral frequency shift can be decomposed into a Fourier series. It has been shown that the Fourier method reproduces forces with higher accuracy compared to the Sader and matrix methods, especially at the local extrema of force curves.[32] Until now, the Fourier method was used only for monomodal AFM operation and the lateral oscillation of the cantilever in combination with a qPlus sensor. We assume that the same approach can be adapted for the deconvolution of lateral forces involved in the torsional cantilever oscillation. Additionally, we extended the Fourier method for the bimodal operation by modifying the formulae according to the bimodal approximation.[7, 21, 46] In general, the tip–sample forces can be determined from

$$F_{\mathrm{ts}}(x)=\sum_{n=1}^{N}-a_{\mathrm{n}}\frac{2\pi n}{L}\cos\left(\frac{2\pi n}{L}x\right)+b_{\mathrm{n}}\frac{2\pi n}{L}\sin\left(\frac{2\pi n}{L}x\right) \tag{3}$$

as described in detail elsewhere, where L is the line length and N is the Nyquist frequency, which is half of the sampling rate s[32]

$$N=\frac{s}{2L} \tag{4}$$

The difference between the monomodal and bimodal approaches appears in the prefactors a_n and b_n in Equations (5)–(8)

$$a_{\mathrm{n\,(mono)}}=-\frac{2k_{\mathrm{tor}}}{f_{0(\mathrm{tor})}}\alpha_{\mathrm{n}}\left(\frac{A_{\mathrm{tor}}L}{4\pi n}\right)\frac{1}{J_1\left(\frac{2\pi nA_{\mathrm{tor}}}{L}\right)} \tag{5}$$

$$b_{\mathrm{n\,(mono)}}=-\frac{2k_{\mathrm{tor}}}{f_{0(\mathrm{tor})}}\beta_{\mathrm{n}}\left(\frac{A_{\mathrm{tor}}L}{4\pi n}\right)\frac{1}{J_1\left(\frac{2\pi nA_{\mathrm{tor}}}{L}\right)} \tag{6}$$

$$a_{\mathrm{n\,(bi)}}=-\frac{2k_{\mathrm{i}}}{f_{0(\mathrm{i})}}\alpha_{\mathrm{n}}\left(\frac{L}{2\pi n}\right)^2\frac{1}{J_0\left(\frac{2\pi nA_{\mathrm{tor}}}{L}\right)} \tag{7}$$

$$b_{n\,(bi)}=-\frac{2k_{i}}{f_{0(i)}}\beta_{n}\left(\frac{L}{2\pi n}\right)^2\frac{1}{J_0\left(\frac{2\pi nA_{tor}}{L}\right)} \tag{8}$$

where J_0 and J_1 are the Bessel functions of the first kind (J) of zero and first order, respectively and i represents the eigenmode which was additionally used for bimodal imaging in frequency modulation. Details about determining a_n and b_n in the bimodal case are provided in the Supporting Information. As in the work of Seeholzer et al.,[32] the factors α_n and β_n are determined from the scalar projection of the data on the relevant sine or cosine function divided by a normalization factor. To control the precision to which the Fourier method can reproduce the original frequency-shift data, it is helpful to calculate additional validation images of the frequency-shift data using

$$\begin{aligned}\Delta f_{\mathrm{mono\,(val)}}(x)=\frac{f_{0(\mathrm{i})}}{2k_{\mathrm{i}}}\sum_{n=1}^{N}&-a_{\mathrm{n}}\left(\frac{4\pi n}{A_{\mathrm{tor}}L}\right)\sin\left(\frac{2\pi n}{L}x\right)J_1\left(\frac{2\pi nA_{\mathrm{tor}}}{L}\right)\\&-b_{\mathrm{n}}\left(\frac{4\pi n}{A_{\mathrm{tor}}L}\right)\cos\left(\frac{2\pi n}{L}x\right)J_1\left(\frac{2\pi nA_{\mathrm{tor}}}{L}\right)\end{aligned} \tag{9}$$

$$\begin{aligned}\Delta f_{\mathrm{bi\,(val)}}(x)=\frac{f_{0(\mathrm{i})}}{2k_{\mathrm{i}}}\sum_{n=1}^{N}&-a_{\mathrm{n}}\left(\frac{2\pi n}{L}\right)^2\sin\left(\frac{2\pi n}{L}x\right)J_0\left(\frac{2\pi nA_{\mathrm{tor}}}{L}\right)\\&-b_{\mathrm{n}}\left(\frac{2\pi n}{L}\right)^2\cos\left(\frac{2\pi n}{L}x\right)J_0\left(\frac{2\pi nA_{\mathrm{tor}}}{L}\right)\end{aligned} \tag{10}$$

To implement the formulas numerically, the MATLAB code provided by Seeholzer et al. was used and extended for the bimodal case. Unlike Seeholzer and co-workers who determined the lateral forces acting between tip and sample while moving over an adsorbate, we aimed to determine the forces that occur during scanning on an HOPG surface. Therefore, it must be considered that the Fourier method is based on the assumption that the frequency-shift data start and end with 0 Hz. Because this is not necessarily the case for the frequency-shift data measured while scanning an HOPG surface, applying the algorithm to the data shifts the average frequency-shift data to 0 Hz, and therefore a relevant amount of force might be neglected. For now, we can correct for this discrepancy by adding manually the offset force determined from the spectroscopic force–distance data. Also, note that i) the Fourier method is limited to the analysis of periodic structures that are larger than the torsional oscillation amplitude, ii) the number of pixels collected during imaging is essential for the success of the Fourier algorithm, and iii) due care must be taken in using the Fourier method for the bimodal approach because we know from the spectroscopic experiments that the flexural amplitude is larger compared to the torsional one. However, as stated in the section entitled "Force reconstruction using Sader method" we assume that the approach is valid because of the different

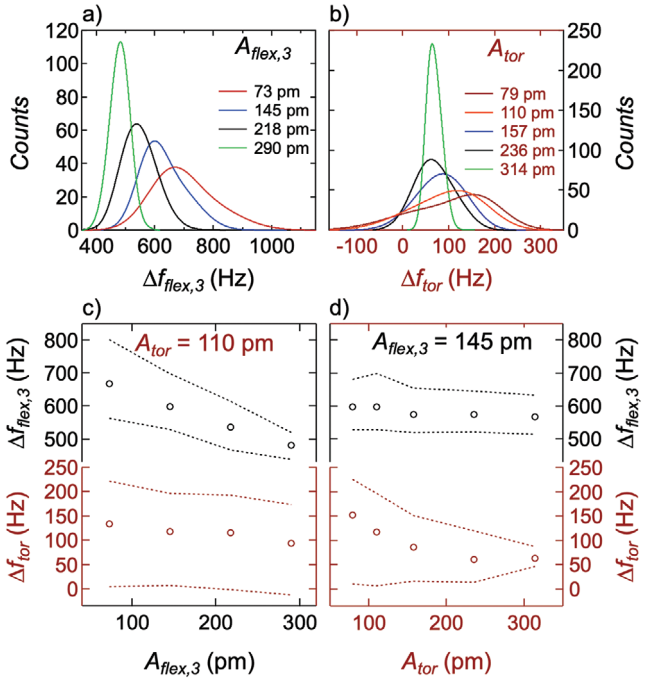

Figure 4. Influence of torsional and third-eigenmode flexural-oscillation amplitudes on observed frequency shifts at a second-flexural-eigenmode amplitude setpoint of 110 pm. a) Histograms of third-eigenmode flexural-frequency-shift images for different third-eigenmode flexural amplitudes. b) Histograms of torsional-frequency-shift images for different torsional amplitudes. Third-eigenmode flexural and torsional frequency shifts at maximum counts (open circles) and at full width at half-maximum (FWHM) (dashed lines) as a function of c) third-flexural-eigenmode amplitude at constant torsional-eigenmode amplitude of 110 pm and d) torsional-eigenmode amplitude at constant third-flexural-eigenmode amplitude of 145 pm.

oscillation directions in space. To corroborate this assumption, we analyzed the frequency-shift histograms of several images (HOPG, 5 nm × 5 nm) taken with systematically changed amplitude values for the torsional eigenmode and the third flexural eigenmode, and the results are shown in **Figure 4**.

2.5. Flexural and Torsional Eigenmode Analysis

In Figure 4a,b, we show histograms of the frequency-shift values from images taken at a constant second-eigenmode amplitude setpoint of 120 pm. The histograms in Figure 4a represent the distribution of the third-eigenmode flexural frequency shift with increasing third-eigenmode flexural amplitude (73–290 pm) at a constant torsional-eigenmode amplitude of approximately 110 pm. The histograms in Figure 4b represent the distribution of the torsional frequency shift with increasing torsional-eigenmode amplitude (79–314 pm) at a constant third-eigenmode flexural amplitude of 145 pm. In Figure 4c,d, the corresponding frequency shifts at the maximum positions of the histograms in Figure 4a,b are shown as open circles, and the frequency shifts at full width at half-maximum (FWHM) are shown with dashed lines. Additionally, the cross-talk behavior between the torsional and third flexural frequency shifts and amplitudes was analyzed. Figure 4c shows that varying the third-flexural-eigenmode amplitude from 73 to 290 pm has little influence on the torsional-frequency-shift histogram, and Figure 4d shows that varying the torsional amplitude from 79 to 314 pm also has no significant influence on the third-eigenmode flexural frequency shift. However, we see that the frequency-shift values at maximum counts decrease with increasing amplitude, and the corresponding FWHM values decrease with increasing amplitude. Note the linear decrease for the third flexural frequency shift, whereas the torsional frequency shift seems to reach a plateau for torsional amplitudes of 157–236 pm. This seems reasonable because in this range the tip moves across more than one carbon hexagon during one oscillation cycle. Surprisingly, it was still feasible to achieve atomic resolution in the torsional-frequency-shift channel if the direction of torsional oscillation was along the zigzag direction of the carbon hexagons. However, no honeycomb structure was resolved for torsional amplitudes larger than the interatomic spacing of the carbon atoms in zigzag direction. We assume that this originates from the symmetry along this direction, which allows lattice resolution, although the torsional amplitude was larger compared to the interatomic spacings. This observation also helped us to determine the torsional oscillation sensitivity, such as described in more detail in the Experimental Section and in the Supporting Information. Another interesting observation was the increasing asymmetry of the peaks in the histograms in Figure 4a,b when decreasing the amplitude of the third flexural eigenmode or the torsional eigenmode, respectively, although the same position was scanned. Surprisingly, the frequency shift at maximum counts was shifted to less-repulsive flexural frequency shifts such as shown in Figure 4a,c, whereas with decreasing amplitude it was shifted to more-repulsive torsional frequency shifts such as shown in Figure 4b,d. We interpret this as another indicator for the independence of the oscillations of the torsional and third flexural eigenmodes and therefore the validity of the bimodal approximation. It impressively demonstrates that for larger third-flexural-eigenmode amplitudes, attractive long-range van der Waals forces become increasingly dominant, which is not the case for sensing the in-plane interactions because of the (relatively) steady oscillation distance with respect to the HOPG surface. Consequently, the monomodal Fourier method[32] allows us to determine in-plane forces along the direction of the torsional oscillation based on the torsional-eigenmode frequency-shift data. The modified bimodal Fourier method can be used to calculate forces that are directed out of plane from the third-eigenmode frequency-shift data along the direction of the torsional-eigenmode oscillation.

2.6. Application of Fourier Method to HOPG Frequency-Shift Images for In-Plane and Out-of-Plane Force Reconstruction

In **Figure 5**, we show images of the forces a,b,e,f) deconvoluted from frequency-shift images, as well as the validation images of the torsional c,d) and third flexural frequency shift g,h) on HOPG using the Fourier method. The red-framed images a–d) were calculated from the frequency-shift images shown in Figure 2. Here, the deconvolution direction was from top to bottom because the

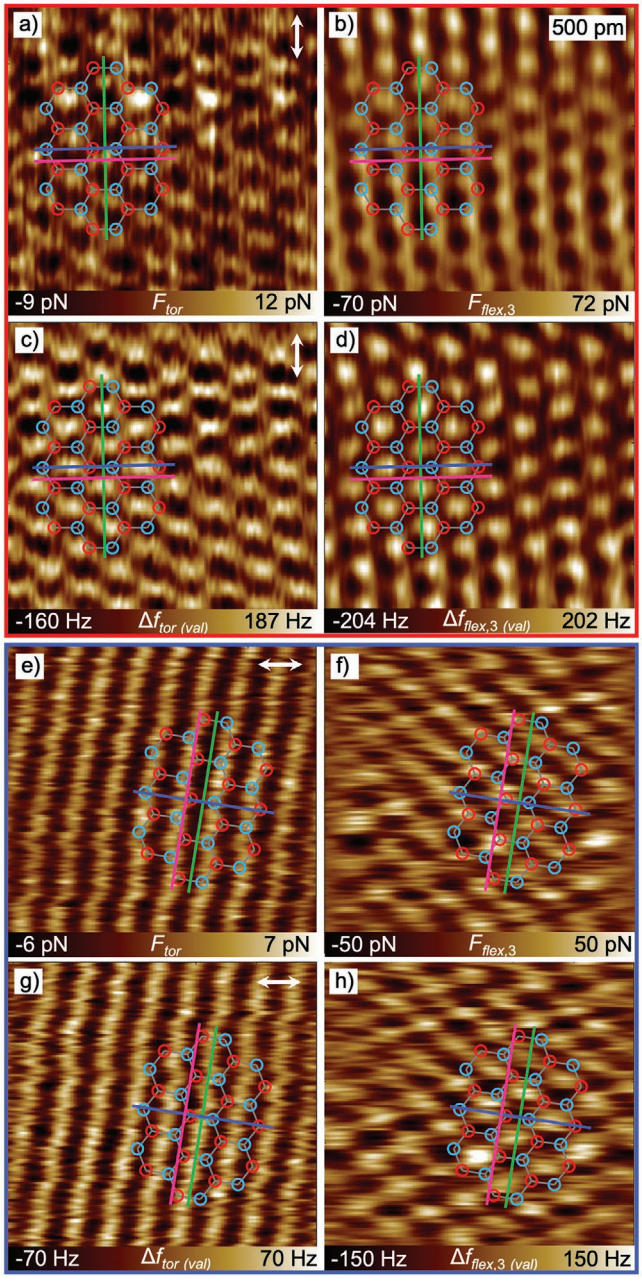

Figure 5. a,b,e,f) Forces and c,d,g,h) frequency-shift validation data determined from frequency-shift images using the Fourier method without offset correction. a,c,e,g) Torsional data were calculated using the monomodal Fourier method, b,d,f,h) flexural data were calculated using the bimodal Fourier method. Red: scan angle = 0°, A_{tor} = 80 pm, $A_{flex,2}$ = 100 pm, $A_{0(flex,2)}$ = 770 pm, $A_{flex,3}$ = 220 pm. Blue: scan angle = 90°, A_{tor} = 110 pm, $A_{flex,2}$ = 90 pm, $A_{0(flex,2)}$ = 770 pm, and $A_{flex,3}$ = 150 pm.

image was taken with a scan angle of 0°. This resulted in a cantilever torsional-oscillation direction (indicated by the white arrows in Figure 5a,c) that was perpendicular to the fast scan axis. The blue-framed images e–h) were deconvoluted from left to right because the scan angle was 90°. This resulted in a cantilever torsional-oscillation direction (indicated by the white arrows in Figure 5e,g) that was parallel to the fast scan axis.

Figure 5 shows that the deconvolution of forces from frequency-shift images was successful. The frequency-shift validation images calculated from Equations (9) and (10) show a constant frequency-shift offset relative to the original frequency-shift images, but the contrast is reproduced with satisfying accuracy (compare Figure 2b,c and Figure 5c,d). The comparison results in a torsional frequency-shift offset of 72 Hz and a flexural frequency-shift offset of 742 Hz. Very similar offset values (74 and 736 Hz, respectively) were determined for the blue-framed images, where the torsional oscillation direction was perpendicular to the fast scan axis. Consequently, an offset value of ≈8 pN must be added to the torsional forces and ≈480 pN to the flexural forces.

Although the angle between the fast scan axis and the orientation of the carbon hexagons was very similar (≈10° deviation) for the red-framed images (Figure 5a–d) and the blue-framed ones (Figure 5e–h), we can observe clear differences in the contrast formation. This might be partially due to the slightly different imaging parameters, but we assume that most of the variations can be attributed to the difference in the torsional oscillation direction relative to the carbon hexagons. This assumption was corroborated by the observation that the differences between the torsional frequency-shift images in Figure 5c,g are much more pronounced compared to those between the flexural frequency-shift images shown in Figure 5d,h. The most reasonable explanation for the striped appearance of the contrast in the torsional force and frequency-shift images in Figure 5e,g is the larger torsional amplitude (≈30%) compared to the amplitude set for the torsional images in Figure 5a,c. From this consideration, the striped appearance of the torsional frequency-shift images would originate from lateral averaging, although note that we never observed atomically resolved contrast when the torsional oscillation direction was oriented along the armchair direction of the carbon hexagons. Obviously, the frequency-shift images and the force images are displaced slightly along the direction of the torsional oscillation, and this is a direct consequence of the relationship between force and frequency shift such as introduced by Giessibl[54] and Sader and Jarvis.[43] Interestingly, we can observe an inversion of the contrast in the flexural-force image (Figure 5b) compared to the flexural-frequency-shift image (Figure 5d). This seems counterintuitive at first glance, but it is rational considering that the force is influenced predominantly by the gradient of the frequency shift. To compare the force and frequency-shift data directly, we took cross sections along the green, pink, and blue lines marked in Figure 5, and the results are shown in **Figure 6**. The frequency-shift cross sections were determined from the original data. The frequency-shift validation data and the original data are compared in Figures S6 and S7 in the Supporting Information.

First, we analyzed the cross-sectional profiles (solid gray) of the frequency shifts shown in Figure 6a,c,d,f, which correspond to the green and blue lines marked in Figure 5c,d,e,h. As discussed in the previous sections and confirmed by the cross sections, the flexural frequency-shift maxima and minima (marked by gray dashed vertical lines) appear at the hollow sides and at the carbon bonds, respectively. Interestingly, it was feasible to distinguish between the atomic sides (red and light-blue dashed vertical lines) from the blue cross section (Figure 6c)

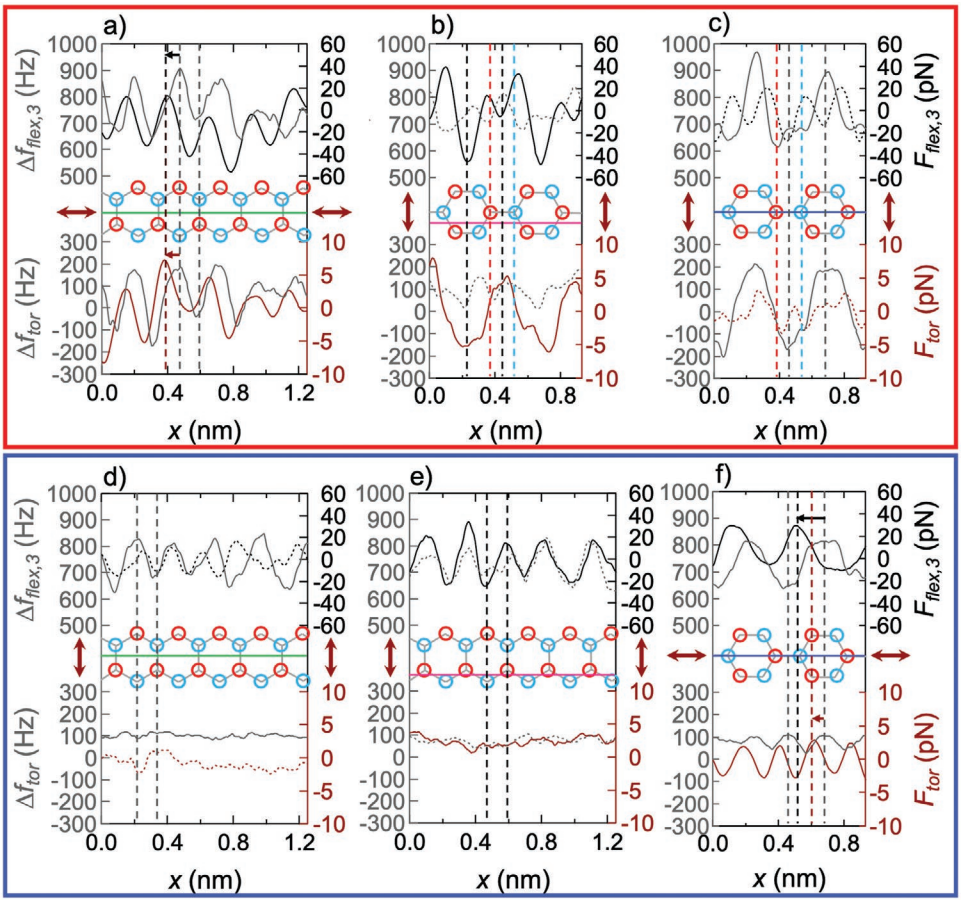

Figure 6. Cross-sectional profiles through force and frequency-shift images of HOPG along the green, pink, and blue lines in Figure 5. Profiles and axis labels are shown in gray for the frequency shift, black for the flexural forces, and red for the torsional forces. The vertical dashed lines mark the positions of characteristic local extrema of the profiles, following the same color code. The torsional oscillation was aligned approximately along the zigzag (resp. armchair) direction of the carbon hexagons for the cross sections shown within the red frame a–c) (resp. blue frame d–f)). The cross sections in (a), (d), and (e) are in the zigzag direction of the carbon hexagons, and those in (b), (c), and (e) are in the armchair direction. The cross sections marked a,d) green and c,f) blue cut the center of the hollow side, whereas those marked b,e) pink are offset from the center of the hollow side by the particular torsional amplitude values to enable analysis of force extrema (black and red arrows).

through the flexural frequency-shift image by the local maxima or minima, respectively, which are different in magnitude. In contrast, the atomic sides could not be discriminated in the corresponding flexural frequency-shift images of Figure 2c (original) and Figure 5d (validation). The capability to discriminate between the atomic sides when imaging HOPG originates from the Bernal stacking of the carbon layers[9] (see schematic in Figure 1). This observation helps to explain the contrast inversion of the flexural-force image in Figure 5b compared to the flexural frequency-shift image in Figure 5d, which can be attributed to the existence of additional maxima and minima. The torsional frequency-shift maxima appear at the hollow sides in Figure 6a,c, if the torsional oscillation direction was along the zigzag direction of the carbon hexagons. Interestingly, we observe negative torsional frequency-shift values at the locations of the carbon bonds. This is surprising if we consider that the flexural frequency shift appears exclusively repulsive. On the other hand, such a behavior of the lateral frequency shift was also observed by Weymouth et al.[55] on the carbon bonds of 3,4,9,10-perylenetetracarboxylic dianhydride (PTCDA). A completely different distribution was observed if the torsional oscillation direction was approximately along the armchair direction of the carbon bonds, such as visible in Figure 6d,f. The torsional frequency shift in Figure 6d is approximately constant, whereas we observe an extra maximum at the position of the carbon bonds in Figure 6f, which corresponds to the position of the minimum flexural frequency shift (see gray dashed vertical lines). As discussed in the section entitled "Application of Fourier method to HOPG frequency-shift images for in-plane and out-of-plane force reconstruction" this might be a consequence of the torsional oscillation amplitude, which was 30 pm larger for the images and cross sections shown in the blue frames in Figures 5e–h and 6d,e (A_{tor} = 110 pm) compared to the images and cross sections shown in the red frames in Figures 5a–d and 6a–c (A_{tor} = 80 pm). We assume that the smaller the oscillation amplitude in the lateral direction, the more sensitive the tip becomes to local variations in the interaction potential. This argument is corroborated by the observation that the torsional frequency shift does not sense attractive interactions for the images shown in Figure 6d,f, which

indicates that the tip interacts with more than one carbon hexagon during one oscillation cycle.

From Figure 6a,f, it can be deduced that the shift of the flexural-force maxima relative to the frequency-shift maxima along the torsional oscillation direction (marked by black arrows and dashed lines) is approximately as large as the particular torsional amplitude (80 pm in Figure 6a and 110 pm in Figure 6f). This is also the case for the torsional-force profiles in Figure 6a, whereas the shift between torsional-force and frequency-shift profiles in Figure 6f is approximately half as large as the torsional amplitude (marked by red arrows and dashed lines). As a consequence, if the cross sections are drawn perpendicular to the torsional oscillation direction and through the center of the hollow sides (extrema of the frequency shift) such as indicated in Figure 6c,d (red/black dotted profiles), the curves do not include the force maxima and minima. Therefore, we show the frequency shifts as solid profiles and the forces as dotted profiles for the cross sections in Figure 6c (blue) and d (green). We additionally drew the cross sections marked in pink in Figure 6b,e, which are shifted from the center of the hollow side by the value of the particular torsional-oscillation amplitude. Thus, the profiles along the pink cross sections allow for the analysis of the force extrema (solid profiles) and do not include the extreme values of the frequency shifts (dotted profiles).

The maximum flexural forces in Figure 6b, originating from the carbon atoms, are distinguishable for the different atomic sides (red and blue vertical dashed lines). This appears nonintuitive at first glance because previously we always found that the maximum frequency shifts take place at the hollow sides rather than at the position of the carbon atoms. The contrast inversion originates from the direction dependence of the algorithm behind the Fourier method. In other words, if the algorithm is applied from top to bottom of the image instead from bottom to top, the force image will appear inverted. For the quantitative interpretation of the force deconvoluted with the Fourier method, it has to be considered that forces do not reflect absolute values but relative differences between the atomic sides. To this end, the mean values and standard deviations of the different local extrema of the forces were determined from the number of values that appear over a cross-sectional length of 2 nm. Consequently, from the black solid profile in Figure 6b we can determine the flexural-force difference between the red and blue marked atoms to be 24 ± 4 pN. The force difference between the blue marked atom and the hollow side is 81 ± 4 pN, and that between the red marked atom and the hollow side is 57 ± 4 pN. The force difference between the center of the carbon bond and the hollow side is 48 ± 5 pN if determined from Figure 6b and 44 ± 10 pN if determined from Figure 6a, being a good match. Compared to similar studies from the literature on pentacene molecules,[26] the determined values are in good agreement but are slightly larger than the literature value (≈37 pN). For the torsional forces, we can measure a force difference of 10 ± 2 pN between the carbon bonds (red dashed line) and the hollow sides for Figure 6a and of 11 ± 2 pN for Figure 6b if the torsional oscillation direction was along the zigzag direction of the carbon bonds. From Figure 6e, we observe that the flexural-force difference between the carbon bonds and the hollow sides is 48 ± 9 pN, and from Figure 6f the force difference was measured as 41 ± 10 pN. The torsional force difference between the hollow sides and the carbon bonds can be determined from Figure 6f as 5 ± 1 pN if the torsional oscillation direction was approximately along the armchair direction of the carbon bonds. From the cross sections shown in Figure 6e, it was not possible to determine reliable torsional force-difference values because of the striped pattern of the frequency-shift distribution as discussed in the previous section. Consequently, the flexural-force differences between the carbon bonds and the hollow sides are in good agreement, regardless of the direction of the torsional oscillation. Interestingly, torsional forces between the different sides differ remarkably depending on the direction of the torsional oscillation relative to the orientation of the carbon hexagons (armchair or zigzag). To gain more understanding of the torsional frequency-shift and respective force images, it might help to consider symmetry reasons for the direction of the torsional oscillation with respect to the alignment of the carbon hexagons. Although the torsional oscillation amplitude is very small, the tip interacts with several atoms of the hexagonal lattice during one cycle. For the alignment of the carbon hexagons with respect to the tip oscillation as shown in the schemes of Figure 6a–c (zigzag orientation), we observe very high symmetry, i.e., along the drawn cross sections, the tip senses the same atom sides (red and blue) during both oscillation half cycles. If the torsional oscillation direction is oriented along the armchair direction of the carbon hexagons as shown in Figure 6d–f, this symmetry is broken. This explains the striped appearance of the frequency-shift and force images. On the other hand, it is reasonable to believe and highly expected to sense differences in the local in-plane forces depending on the oscillation direction relative to the orientation of the carbon hexagons. Although the elastic constants of graphite do not imply an in-plane anisotropy,[56] in-plane forces determined locally on the atomic scale can differ depending on the oscillation direction because of the different numbers of carbon bonds involved, as demonstrated in the present study.

3. Conclusion

Force quantification by AFM is indispensable for understanding the mechanical characteristics of materials, in particular at the atomic scale and in air under ambient conditions. We presented a multifrequency methodology that simultaneously determines the in-plane and out-of-plane force differences within the topmost graphene layer of HOPG with atomic resolution. By analyzing the mean deflection of the cantilever, we showed that this graphene layer is lifted locally from the bulk by the exerted tip forces that exceed the weak van der Waals interactions between the basal planes. This effect must be addressed when analyzing forces from dynamic force spectroscopy data. In addition, we detected a comparably large hysteretic behavior between approach and retract curves on HOPG in air under ambient conditions. This was partially assigned to the presence of water films on the surface, but we assume that hysteresis originates mainly from the local lift of the topmost carbon layers, which complicates interpretation of spectroscopic data. We showed that the in-plane force differences between carbon bonds or carbon atoms and the hollow sides exist depending on the alignment of

the shear direction relative to the alignment of the carbon bonds. In contrast, the force differences in the out-of-plane direction are independent of the shear direction. To quantify atom-atom interactions, we presumed validity of the bimodal approximation for lateral tip oscillations. As a key result, we determined the in-plane force between carbon bonds and hollow sides to be 11 ± 2 or 5 ± 1 pN when shearing carbon hexagons along the zigzag or armchair direction, respectively. This shows the strong anisotropic mechanical behavior of HOPG at the atomic level that must be considered when designing graphene-based nanomaterials.

4. Experimental Section

Sample: The HOPG sample (grade 2) was purchased from SPI Supplies (Structure Probe, Inc., West Chester, PA, USA) and had a mosaic spread angle of as little as $0.8 \pm 0.2°$. Prior to the AFM experiments, it was cleaved with adhesive tape in air under ambient conditions to expose a fresh clean surface.

Cantilevers: Supersharp cantilevers of the type HiResC15/Cr-Au were purchased from Mikromasch (Innovative Solutions Bulgaria Ltd., Sofia, Bulgaria). The cantilevers used for the experiments shown in this study were chosen to exhibit very similar force constants and free vibration resonance frequencies (≤2% relative aberration). Representative values of the resonance frequencies were $f_{0(\mathrm{flex},1)} = 266$ kHz, $f_{0(\mathrm{flex},2)} = 1.67$ MHz, $f_{0(\mathrm{flex},3)} = 4.62$ MHz, and $f_{0(\mathrm{tor})} = 1.73$ MHz. The respective force constants were determined as $k_{\mathrm{flex},1} = 26$ N m^{-1}, $k_{\mathrm{flex},2} = 644$ N m^{-1}, $k_{\mathrm{flex},3} = 3489$ N m^{-1}, and $k_{\mathrm{tor}} = 472$ N m^{-1} (details are given in the Supporting Information). The manufacturer assures a tip radius of <1 nm realized by an extra tip consisting of hydrophobic DLC.

Environmental Conditions: The temperature in the AFM chamber while imaging was 26–27 °C, and the relative humidity was 22–31% for the different experiments. Neither the temperature nor the relative humidity was actively controlled, but the imaging conditions remained stable during imaging.

Trimodal AFM Setup: Experiments were performed with a Cypher S atomic force microscope (Asylum Research, Oxford Instruments, Santa Barbara, CA, USA) equipped with a blueDrive photothermal excitation of the cantilever. The torsional and third-eigenmode flexural frequency shifts were tracked with additional phase-locked loops (HF2PLL, Zurich Instruments, Zurich, Switzerland). The gains of the PLLs (P = 45–46, I = 32 000–49 000 for the cantilever used) were adjusted following numbers suggested by the "PLL Advisor" of the ziControl software (Zurich Instruments, Zurich, Switzerland), providing stable tracking of the torsional and the third flexural eigenmode resonance frequencies. Proper gains for the amplitude feedback (constant-amplitude frequency modulation, $P = 1$, I = 1000–4000) were sought by toggling the setpoint amplitude between two values (typically in the range of ±50% of the measurement setpoint amplitude) ensuring that the time signal resulted in a decent rectangular shape. Two PID controllers built into the same instrument were used to adjust the drive amplitudes to maintain constant torsional and third-eigenmode flexural amplitudes.

Calibration of Torsional Inverse Optical Lever Sensitivity: First, the torsional force constant of the cantilever was determined using the Sader method.[57,58] Subsequently, the calibration of the torsional resonance invOLS was accomplished by fitting the torsional resonance peak in the lateral thermal noise spectrum to the algorithm developed in refs. [59,60]. However, it needs to be mentioned that the determination of the torsional force constant using the Sader method is prone to errors due to the strong dependency of the obtained values on the dimensions of the cantilever. Hence, the torsional invOLS value was corrected based on the results of the histogram analysis in Figure 4b,d. It is assumed that an asymmetric peak distribution in the histogram is a strong indication of a sufficiently small torsional amplitude reflecting values smaller than the interatomic spacing of carbon atoms. Hence, the transition between the torsional amplitudes corresponding to symmetric and asymmetric histograms was taken as reference value where the oscillation matches the interatomic spacing of carbon atoms in zigzag direction. Further details on the calibration procedure are given in the Supporting Information.

Data Processing: The topography images shown were first-order flattened to remove any tilt from the images using the Igor Pro v6.36 software (WaveMetrics Inc., Lake Oswego, OR, USA). All images resulting directly from AFM measurements were treated with a 3×2 Gauss filter to remove noise from the images. This step was additionally required to enable the successful application of the Fourier method. MATLAB R2018a (MathWorks Inc., Natick, MA, USA) was used for the implementation of the Fourier method into a program code based on the script provided by Seeholzer et al.[32] Subsequently, the calculated force images were smoothed with a Savitzky–Golay filter over nine points with a first-order polynomial. The same smoothing procedure was accomplished to reduce noise in the cross sections shown.

Supporting Information

Supporting Information is available from the Wiley Online Library or from the author.

Acknowledgements

The authors thank Niklas Scheer for helping with the MATLAB code and the Deutsche Forschungsgemeinschaft (Project number 407750697) for financial support.

Open access funding enabled and organized by Projekt DEAL.

Conflict of Interest

The authors declare no conflict of interest.

Data Availability Statement

Research data are not shared.

Keywords

atomic resolution, force deconvolution, highly oriented pyrolytic graphite, in-plane and out-of-plane forces, trimodal atomic force microscopy

Received: July 20, 2021
Revised: August 27, 2021
Published online: September 29, 2021

[1] T. C. Fu, Y. Cheng, A. Li, H. Liu, Z. Cheng, P. Li, J. Liu, *Sens. Actuators, B* **2021**, *344*, 130260.
[2] S. W. Chen, Z. Cheng, J. Liu, *Sens. Actuators, B* **2020**, *320*, 128430.
[3] J. Phiri, P. Gane, T. C. Maloney, *Mater. Sci. Eng., B* **2017**, *215*, 9.
[4] A. Zandiatashbar, G. H. Lee, S. J. An, S. Lee, N. Mathew, M. Terrones, T. Hayashi, C. R. Picu, J. Hone, N. Koratkar, *Nat. Commun.* **2014**, *5*, 3186.
[5] I. W. Frank, D. M. Tanenbaum, A. M. Van der Zande, P. L. McEuen, *J. Vac. Sci. Technol., B: Microelectron. Nanometer Struct.–Process., Meas., Phenom.* **2007**, *25*, 2558.
[6] F. Cellini, Y. Gao, E. Riedo, *Sci. Rep.* **2019**, *9*, 4075.

[7] S. Kawai, T. Glatzel, S. Koch, B. Such, A. Baratoff, E. Meyer, *Phys. Rev. B* **2010**, *81*, 085420.
[8] A. Schwarz, U. D. Schwarz, S. Langkat, H. Hölscher, W. Allers, R. Wiesendanger, *Appl. Surf. Sci.* **2002**, *188*, 245.
[9] H. Holscher, W. Allers, U. D. Schwarz, A. Schwarz, R. Wiesendanger, *Phys. Rev. B* **2000**, *62*, 6967.
[10] S. Hembacher, F. J. Giessibl, J. Mannhart, C. F. Quate, *Proc. Natl. Acad. Sci. USA* **2003**, *100*, 12539.
[11] B. J. Albers, M. Liebmann, T. C. Schwendemann, M. Z. Baykara, M. Heyde, M. Salmeron, E. I. Altman, U. D. Schwarz, *Rev. Sci. Instrum.* **2008**, *79*, 033704.
[12] S. A. L. Weber, J. I. Kilpatrick, T. M. Brosnan, S. P. Jarvis, B. J. Rodriguez, *Nanotechnology* **2014**, *25*, 175701.
[13] F. J. Giessibl, *Appl. Phys. Lett.* **2000**, *76*, 1470.
[14] D. S. Wastl, A. J. Weymouth, F. J. Giessibl, *ACS Nano* **2014**, *8*, 5233.
[15] F. J. Giessibl, M. Herz, J. Mannhart, *Proc. Natl. Acad. Sci. USA* **2002**, *99*, 12006.
[16] D. Kirpal, J. Qiu, K. Pürckhauer, A. J. Weymouth, M. Metz, F. J. Giessibl, *Rev. Sci. Instrum.* **2021**, *92*, 043703.
[17] F. J. Giessibl, *Rev. Sci. Instrum.* **2019**, *90*, 011101.
[18] S. Kawai, S.-i. Kitamura, D. Kobayashi, S. Meguro, H. Kawakatsu, *Appl. Phys. Lett.* **2005**, *86*, 193107.
[19] S. Kawai, H. Kawakatsu, *Appl. Phys. Lett.* **2006**, *89*, 013108.
[20] V. V. Korolkov, I. G. Timokhin, R. Haubrichs, E. F. Smith, L. X. Yang, S. H. Yang, N. R. Champness, M. Schroder, P. H. Beton, *Nat. Commun.* **2017**, *8*, 1385.
[21] S. Kawai, T. Glatzel, S. Koch, B. Such, A. Baratoff, E. Meyer, *Phys. Rev. Lett.* **2009**, *103*, 220801.
[22] E. J. Miller, W. Trewby, A. F. Payam, L. Piantanida, C. Cafolla, K. Voitchovsky, *JoVE—J. Visualized Exp.* **2016**, *118*, e54924.
[23] T. Meier, B. Eslami, S. D. Solares, *Nanotechnology* **2016**, *27*, 085702.
[24] L. Gross, F. Mohn, N. Moll, P. Liljeroth, G. Meyer, *Science* **2009**, *325*, 1110.
[25] N. Moll, L. Gross, F. Mohn, A. Curioni, G. Meyer, *New J. Phys.* **2010**, *12*, 125020.
[26] C.-S. Guo, M. A. Van Hove, X. Ren, Y. Zhao, *J. Phys. Chem. C* **2015**, *119*, 1483.
[27] M. R. Uhlig, D. Martin-Jimenez, R. Garcia, *Nat. Commun.* **2019**, *10*, 2606.
[28] T. Fukuma, R. Garcia, *ACS Nano* **2018**, *12*, 11785.
[29] K. Umeda, L. Zivanovic, K. Kobayashi, J. Ritala, H. Kominami, P. Spijker, A. S. Foster, H. Yamada, *Nat. Commun.* **2017**, *8*, 2111.
[30] A. M. Sweetman, S. P. Jarvis, H. Sang, I. Lekkas, P. Rahe, Y. Wang, J. Wang, N. R. Champness, L. Kantorovich, P. Moriarty, *Nat. Commun.* **2014**, *5*, 3931.
[31] M. Z. Baykara, T. C. Schwendemann, B. J. Albers, N. Pilet, H. Monig, E. I. Altman, U. D. Schwarz, *Nanotechnology* **2012**, *23*, 405703.
[32] T. Seeholzer, O. Gretz, F. J. Giessibl, A. J. Weymouth, *New J. Phys.* **2019**, *21*, 083007.
[33] D. Ebeling, B. Eslami, S. D. J. Solares, *ACS Nano* **2013**, *7*, 10387.
[34] S. D. Solares, G. Chawla, *Meas. Sci. Technol.* **2010**, *21*, 125502.
[35] C. Dietz, *Nanoscale* **2018**, *10*, 460.
[36] V. Pini, B. Tiribilli, C. M. C. Gambi, M. Vassalli, *Phys. Rev. B* **2010**, *81*, 054302.
[37] D. Kiracofe, K. Kobayashi, A. Labuda, A. Raman, H. Yamada, *Rev. Sci. Instrum.* **2011**, *82*, 013702.
[38] S. Santos, V. Barcons, H. K. Christenson, D. J. Billingsley, W. A. Bonass, J. Font, N. H. Thomson, *Appl. Phys. Lett.* **2013**, *103*, 063702.
[39] R. Garcia, R. Perez, *Surf. Sci. Rep.* **2002**, *47*, 197.
[40] S. Kawai, T. Glatzel, S. Koch, B. Such, A. Baratoff, E. Meyer, *Phys. Rev. B* **2009**, *80*, 085422.
[41] S. E. Yalcin, B. A. Legg, M. Yeşilbaş, N. S. Malvankar, J.-F. Boily, *Sci. Adv.* **2020**, *6*, eaaz9708.
[42] S. Kawai, H. Kawakatsu, *Phys. Rev. B* **2009**, *79*, 115440.
[43] J. E. Sader, S. P. Jarvis, *Appl. Phys. Lett.* **2004**, *84*, 1801.
[44] F. J. Giessibl, *Appl. Phys. Lett.* **2000**, *78*, 123.
[45] J. E. Sader, S. P. Jarvis, *Phys. Rev. B* **2004**, *70*, 012303.
[46] E. T. Herruzo, R. Garcia, *Beilstein J. Nanotechnol.* **2012**, *3*, 198.
[47] M. D. Aksoy, A. Atalar, *Phys. Rev. B* **2011**, *83*, 075416.
[48] Y. Naitoh, Z. M. Ma, Y. J. Li, M. Kageshima, Y. Sugawara, *J. Vac. Sci. Technol., B* **2010**, *28*, 1210.
[49] M. Chiesa, C.-Y. Lai, *Phys. Chem. Chem. Phys.* **2018**, *20*, 19664.
[50] A. Calo, O. V. Robles, S. Santos, A. Verdaguer, *Beilstein J. Nanotechnol.* **2015**, *6*, 809.
[51] B. A. Krajina, L. S. Kocherlakota, R. M. Overney, *J. Chem. Phys.* **2014**, *141*, 164707.
[52] A. J. Weymouth, D. Meuer, P. Mutombo, T. Wutscher, M. Ondracek, P. Jelinek, F. J. Giessibl, *Phys. Rev. Lett.* **2013**, *111*, 126103.
[53] J. E. Sader, B. D. Hughes, F. Huber, F. J. Giessibl, *Nat. Nanotechnol.* **2018**, *13*, 1088.
[54] F. J. Giessibl, *Phys. Rev. B* **1997**, *56*, 16010.
[55] A. J. Weymouth, E. Riegel, O. Gretz, F. J. Giessibl, *Phys. Rev. Lett.* **2020**, *124*, 196101.
[56] K. H. Michel, B. Verberck, *Phys. Status Solidi B* **2008**, *245*, 2177.
[57] C. P. Green, H. Lioe, J. P. Cleveland, R. Proksch, P. Mulvaney, J. E. Sader, *Rev. Sci. Instrum.* **2004**, *75*, 1988.
[58] R. J. Cannara, M. Eglin, R. W. Carpick, *Rev. Sci. Instrum.* **2006**, *77*, 053701.
[59] M. J. Higgins, R. Proksch, J. E. Sader, M. Polcik, S. Mc Endoo, J. P. Cleveland, S. P. Jarvis, *Rev. Sci. Instrum.* **2006**, *77*, 013701.
[60] N. Mullin, J. K. Hobbs, *Rev. Sci. Instrum.* **2014**, *85*, 113703.